1   **Two years of satellite-based carbon dioxide emission quantification at the world's**

2   **largest coal-fired power plants**

3   Daniel H. Cusworth[1,2], Andrew K. Thorpe[3], Charles E. Miller[3], Alana K. Ayasse[1], Ralph Jiorle[1],

4   Riley M. Duren[1,2,3], Ray Nassar[4], Jon-Paul Mastrogiacomo[5], and Robert R. Nelson[3]

5   [1]Carbon Mapper, Pasadena, CA, USA

6   [2]Arizona Institutes for Resilience, University of Arizona, Tucson, AZ, USA

7   [3]Jet Propulsion Laboratory, California Institute of Technology, Pasadena, CA, USA

8   [4]Environment & Climate Change Canada, Toronto, ON, Canada

9   [5]University of Toronto, Toronto, ON, Canada

11   Corresponding Author: Daniel H. Cusworth (dan@carbonmapper.org)

13   **Abstract**

14   Carbon dioxide (CO_2) emissions from combustion sources are uncertain in many places

15   across the globe. Satellites have the ability to detect and quantify emissions from large CO_2 point

16   sources, including coal-fired power plants. In this study, we made observations with the PRecursore

17   IperSpettrale della Missione Applicativa (PRISMA) satellite imaging spectrometer and the Orbiting

18   Carbon Observatory-3 (OCO-3) instrument onboard the International Space Station at over 30 coal-

19   fired power plants routinely between 2021-2022. CO_2 plumes were detected in 50% of acquired

20   PRISMA scenes, which is consistent with the combined influence of viewing parameters on detection

21   (solar illumination, surface reflectance) and unknown factors (like daily operational status). We

22   compare satellite-derived emission rates to *in situ* stack emission observations and find average

23   agreement to within 27% for PRISMA and 30% for OCO-3, though more observations are needed to

24   robustly characterize the error. We highlight two examples of fusing PRISMA with OCO-2 and

25   OCO-3 observations in South Africa and India. For India, we acquired PRISMA and OCO-3

observations on the same day and use the high spatial resolution capability of PRISMA (30 m spatial/pixel resolution) to partition relative contributions of two distinct emitting power plants to the net emission. Though an encouraging start, two years of observations from these satellites did not produce sufficient observations to estimate annual average emission rates within low (<15%) uncertainties. However, as the constellation of CO_2-observing satellites is poised to significantly improve in the coming decade, this study offers an approach to leverage multiple observation platforms to better quantify and characterize uncertainty for large anthropogenic emission sources.

1 Introduction

Anthropogenic carbon dioxide (CO_2) emissions are dominated by strong discrete point sources: power and other industrial combustion are estimated to make up 59% of global anthropogenic CO_2 emissions with transport, buildings, and other sources making up the remaining 20%, 9%, and 12%, respectively (Crippa et al., 2022). Fossil fuel combustion is the largest contributor to warming trends globally since the pre-industrial era (IPCC, 2021). However, there remains uncertainty in the total magnitude of emissions from these sectors as bottom-up emission estimates rely on reported emission factors and activity data, which may vary in granularity and quality across countries and provinces (Hong et al., 2017; Guan et al., 2017). Accurate CO_2 emission quantification is important in light of the Paris Agreement, as participating countries must develop plans and report progress to reduce their country's greenhouse gas (GHG) emissions (UN, 2015). Leveraging atmospheric measurements, particularly satellite remote sensing, can help reduce uncertainty in facility-level CO_2 emission estimates, provided that the observations are accurate and sufficiently sample the facility in time (Hill and Nassar, 2019). Deployed systematically with robust error characterization, this system could be an anchor towards assessing and verifying anticipated

49 CO$_2$ emission reductions as part of national and global GHG emission reduction plans and

50 agreements.

51   Several studies have shown that atmospheric sounding satellites can accurately quantify some

52 point source CO$_2$ emissions from large individual coal-fired power plants. First, the Orbiting Carbon

53 Observatory-2 (OCO-2; Crisp et al., 2017) is a space-based instrument that observes solar

54 backscattered near-infrared radiance in the oxygen *A* band (758-772 nm; 0.04 nm spectral resolution),

55 the weak CO2 band (1594-1619 nm; 0.08 nm spectral resolution), and strong CO2 band (2042-2082

56 nm; 0.10 nm spectral resolution). OCO-2 views in nadir mode over land, while sun glint mode

57 increases the signal over water giving measurements both land and water, and target mode to target

58 specific validation or calibration sites. With its 10-km wide swath, $\leq$1.3x2.25 km^2 pixel resolution,

59 and better than 1.0 ppm precision for retrievals of the column-mean dry-air mole fraction of CO$_2$

60 (XCO$_2$) (Taylor et al., 2023), OCO-2 is sensitive to single CO$_2$ point sources that emit sufficiently

61 close to an OCO-2 orbital track and are spatially isolated from other major CO$_2$ sources. Using

62 satellite observations from OCO-2, Nassar et al. (2017) detected strong CO$_2$ enhancements in the

63 near vicinity of seven large coal-fired power plants and employed a Gaussian plume model emission

64 quantification technique to estimate emission rates for these facilities. Further study expanded the set

65 of facilities that could be quantified by OCO-2 (Nassar et al., 2021). Other studies have leveraged

66 the nitrogen dioxide (NO$_2$) retrieval capability and wide swath of the TROPOspheric Monitoring

67 Instrument (TROPOMI; van Geffen et al., 2020) to attribute and corroborate strong CO$_2$ signals seen

68 in OCO-2 observations (Hakkarainen et al., 2021; Reuter et al., 2019). The Orbiting Carbon

69 Observatory-3 (OCO-3; Eldering et al., 2019), the flight spare of OCO-2, has been on board the

70 International Space Station (ISS) since May 2019. Like OCO-2, it has been shown capable of

71 quantifying CO$_2$ power plant emissions. Nassar et al. (2022) analyzed nine successful OCO-3

72 acquisitions of the Bełchatów Power Station and found the variability in satellite-based emission

73 estimates agreed well with the variability in independently reported hourly power generation. Guo et

74 al., (2023) estimated emissions at Chinese power plants using OCO-2/3 and found close agreement

75 with emission inventories. OCO-3 is different than OCO-2 in that it has a two-axis Pointing Mirror

76 Assembly (PMA) for more agile pointing, allowing it to rapidly point off-nadir and take Snapshot

77 Area Mapping (SAM) mode observations over the course of two minutes. These SAMs are

78 approximately $80{\times}80$ km^2 collections of measurements and are typically over sites of interest

79 including cities, power plants, volcanoes, and flux towers.

80   Another class of remote sensing imaging spectrometers – sometimes also referred to as

81 hyperspectral imagers – also have been shown capable of detecting and quantifying strong CO_2

82 signals from large point sources. Thorpe et al. (2017) flew the Next-Generation Airborne/Infrared

83 Imaging Spectrometer (AVIRIS-NG) over a coal-fired power plant in Four Corners, New Mexico,

84 and detected strong CO_2 plumes. AVIRIS-NG observes a large range of solar backscattered radiance

85 (380-2500 nm), but at much coarser spectral resolution (5 nm), and high spatial resolution (e.g., 3 m

86 when flown at 3 km altitude). The much finer spatial resolution of AVIRIS-NG allows for improved

87 visualization of the origin of a CO_2 plume, but at the expense of fine precision for a single observed

88 CO_2 column. Still, Cusworth et al. (2021) analyzed a combination of AVIRIS-NG and the identically

89 built Global Airborne Observatory (GAO) at over 20 power plants in the U.S., quantified emission

90 rates, and found close agreement with continuous emissions monitoring (CEMS) hourly emission

91 observations. From space, the PRecursore IperSpettrale della Missione Applicativa (PRISMA),

92 launched in 2019, like AVIRIS-NG and GAO is sensitive to a large range of solar backscattered

93 radiance (400-2500 nm), albeit at coarser spectral and spatial resolution (10 nm spectral resolution;

94 30 m spatial resolution; Loizzo et al., 2018). PRISMA is a tasked satellite instrument potentially

95   capable of hundreds of 30×30 km^2 observations per day, with equatorial crossing time of 10:30am,

96   and target revisit of seven days, though true revisit depends on tasking priorities of the system.

97   Cusworth et al. (2021) showed a few examples of CO_2 plumes detected and quantified with

98   PRISMA, with quantified emissions similar in magnitude to reported CEMS emissions..

99   The capacity for satellites to be leveraged as useful tools for reducing uncertainty in the global

100   CO_2 anthropogenic emission sector requires synthesis and routine observations (i.e., tasking) of a

101   critical number of facilities. Therefore, in this study, we made observations at a subset of global coal-

102   fired power plants routinely over the course of two years to probe detection limits, emission

103   quantification uncertainty, and data yields. We observed these facilities with both OCO-3 and

104   PRISMA. To our knowledge to date, this study represents the largest satellite-based facility scale

105   investigation of direct CO_2 emission quantification across a diverse set of global power plants, and

106   the first investigation to assess the capability of PRISMA to reliably detect and quantify CO_2 point

107   sources. The results, though not sufficient by themselves to reduce uncertainty relative to bottom-up

108   inventories significantly on an annual basis, show a path forward for data fusion and synthesis of

109   observations from the growing constellation of planned CO_2 sensing satellites.

110

111   **2 Methods**

112   Table 1 lists the locations of all power plants we targeted during this study between 2021-

113   2022 with PRISMA. OCO-3 includes a subset of these sites as well as other fossil fuel combustion

114   sites as part of its list of possible targets. We identified coal-fired power plants to routinely target

115   using a combination of bottom-up and top-down information. Bottom-up coal-fired power plant CO_2

116   emission estimates rely on activity data, that usually includes permitted capacity of a power plant

117   and its operational state; and emission factors, usually estimated from the composition of the coal

118 that is combusted. Inventories, like the Global Energy Monitor (GEM), include this data for a large

119 set of coal-fired power plants across the globe (GEM, 2023). From the GEM database, we gathered

120 the top 10 largest bottom-up coal-fired power plants globally. We then gathered a list of top-down

121 TROPOMI NO_2 combustion hotspots, as inferred by Beirle et al. (2021). We included an additional

122 seven unique power plants using this dataset. Because the imaging scene size of PRISMA is 30×30

123 km^2, some adjacent smaller power plants were imaged simultaneously along with these larger power

124 plants. In total, outside of the U.S., we made PRISMA observations at 27 power plants. In the U.S.,

125 we chose 10 power plants to routinely target using reported EPA CEMS information

126 (campd.epa.gov): five of the top 30 emitting power plants, and five progressively lower emitters,

127 chosen so that we could assess satellite detection capabilities.

128

129 Table 1. Power plants that were targeted specifically by PRISMA in this study.

Power Plant Name	Country	Latitude	Longitude	Number clear-sky observations	Number plume detections	Minimum quantified CO_2 emission (kt CO_2 h^{-1})	Mean quantified CO_2 emission (kt CO_2 h^{-1})	Maximum quantified CO_2 emission (kt CO_2 h^{-1})
Mundra-Adani	India	22.82	69.55	12	7	0.49±0.07	1.09±0.19	1.76±0.32
Korba-Balco	India	22.40	82.74	5	1	NA*	NA	NA
PLN Paiton Baru	Indoneisa	-7.71	113.57	4	2	NA	NA	NA
Craig	USA	40.46	-107.59	5	5	0.56±0.11	0.69±0.16	0.8±0.22
Cumberland	USA	36.39	-87.65	1	0	NA	NA	NA
Dry Fork	USA	44.39	-105.46	6	3	0.61±0.09	0.65±0.13	0.69±0.16
H L Spurlock	USA	38.70	-83.82	5	3	1.15±0.32	1.26±0.39	1.37±0.45
Ulsan Hanju (1)	South Korea	35.49	129.33	1	0	NA	NA	NA
Hasdeo	India	22.41	82.69	5	0	NA	NA	NA
Hekinan	Japan	34.83	136.96	6	4	0.72±0.47	3.88±1.09	8.35±2.14
Baotou-1	China	40.66	109.66	5	2	0.19±0.07	0.27±0.07	0.35±0.07
Kendal	South Africa	-26.09	28.97	7	2	0.85±0.13	0.85±0.13	0.85±0.13
NTPC Korba	India	22.39	82.68	6	1	1.28±0.27	1.28±0.27	1.28±0.27

Kriel	South Africa	-26.25	29.18	8	3	0.74±0.15	0.82±0.15	0.95±0.16
Labadie	USA	38.56	-90.84	4	4	0.73±0.18	0.73±0.18	0.73±0.18
Martin Lake	USA	32.26	-94.57	8	8	1.45±0.31	2±0.59	2.6±0.98
Matimba	South Africa	-23.67	27.61	11	8	0.33±0.05	0.72±0.16	1.14±0.32
Matla	South Africa	-26.28	29.14	8	3	0.33±0.05	0.77±0.15	1.37±0.27
Medupi	South Africa	-23.71	27.56	15	12	0.33±0.06	0.83±0.19	1.47±0.34
Mundra-Tata	India	22.82	69.53	12	5	0.38±0.09	0.74±0.13	1.32±0.21
Niederaussem	Germany	51.00	6.67	1	0	NA	NA	NA
Oregon	USA	41.67	-83.44	5	1	NA	NA	NA
Paiton-3	Indonesia	-7.71	113.58	4	4	1.54±0.37	3.16±0.69	4.78±1.02
Rihand	India	24.03	82.79	8	5	0.83±0.17	0.99±0.26	1.36±0.38
Sanfeng	China	40.66	109.76	6	0	NA	NA	NA
Sasan	India	23.98	82.63	9	7	0.65±0.15	1.01±0.24	1.51±0.31
Sooner	USA	36.45	-97.05	6	3	1.05±0.22	1.05±0.22	1.05±0.22
Togtoh	China	40.20	111.36	2	2	0.25±0.06	0.91±0.17	1.58±0.27
Ulsan Hanju (2)	South Korea	35.47	129.38	1	0	NA	NA	NA
Vindhyachal	India	24.10	82.68	9	7	0.33±0.1	0.72±0.15	1.24±0.23
Waigaoqiao	China	31.36	121.60	6	1	NA	NA	NA
Yeosu Hanwha	South Korea	34.84	127.69	2	0	NA	NA	NA
Yosu	South Korea	34.83	127.67	2	0	NA	NA	NA
Al Zour	Kuwait	28.71	48.37	12	0	NA	NA	NA

*A value of "NA" indicates that no plumes were detected at this power plant or that the emission quantification algorithm (described in Methods) failed to quantify an emission rate.

2.1 PRISMA observations and quantification

PRISMA is a tasked satellite instrument, capable of collecting around 200 30×30 km^2 targets per day and has 20° pointing capability off nadir. Authenticated users can program single observation requests through PRISMA's web portal (prisma.asi.it), which currently allows for 13 concurrent requests at a time per user. We specified two-week observing windows for each request, and configured requests to collect if the scene-averaged solar zenith angle (SZA) was less than 70° and

139 forecast meteorology anticipated less than 20% cloud cover. If the orbital configuration, weather,

140 SZA align and there are no other conflicting or higher priority requests, PRISMA images a target.

141 For each acquired PRISMA image, we performed XCO_2 retrievals on all pixels within a 2.5

142 km radius around the power plant. We retrieve XCO_2 using the Iterative Maximum A Posteriori –

143 Differential Optical Absorption Spectroscopy (IMAP-DOAS) algorithm, as implemented in

144 Cusworth et al. (2021). This approach estimates XCO_2 by decomposing an observed radiance

145 spectrum into high and low frequency features between 1900-2100 nm. For high-frequency features,

146 we simulate atmospheric transmission of CO_2, H_2O, and N_2O using a Beer-Lambert approximation.

147 For low-frequency features (e.g., surface reflectance, aerosol scattering), we use an 8-degree

148 polynomial. The forward model that drives IMAP-DOAS therefore has the following form:

149
$$F^h(\mathbf{x}) = I_0(\lambda) \exp\left(-\sum_{n=1}^{6} s_n \sum_{l=1}^{72} A_l \tau_{n,l}\right) \sum_{k=0}^{K} a_k \lambda^k \quad (1)$$

150 Where F^h is simulated backscattered radiance at wavelength λ, I_0 is incident solar intensity, A_l is the

151 airmass factor at vertical level $l \in [1,72]$, $\tau_{n,l}$ is the optical depth for each trace gas element, s_n is the

152 scaling factor applied to the optical depth, and a_k is a polynomial coefficient (K=8). Optical depths

153 are computed by querying meteorological information for pressure and temperature from the

154 MERRA-2 reanalysis (Gelaro et al., 2017), and using that information to select proper HITRAN

155 absorption cross sections for each trace gas (Kochanov et al., 2016). To compare the model from

156 Equation 1 against PRISMA observed radiance ($\mathbf{y}$), we compute $F^h(\mathbf{x})$ between 1900-2100 nm at

157 0.02 nm resolution, then convolve the output using the PRISMA full-width half maximum, and

158 sample at PRISMA wavelength positions. This results in vector $\mathbf{F}(\mathbf{x})$ that is comparable to $\mathbf{y}$. The

159 vector $\mathbf{x}$, also called the state vector, includes scale factors for CO_2, H_2O, N_2O, and polynomial

160 coefficients: $\mathbf{x} = (s_{CO2}, s_{H2O}, s_{N2O}, a_o, \dots, a_8)$.

161   XCO_2 is retrieved from PRISMA radiance using a Bayesian optimal estimation approach

162   (Rodgers, 2000). Here, the optimized state vector solution, or posterior, is solved through Gauss-

163   Newton iteration:

164          $$\mathbf{x}_{i+1} = \mathbf{x_A} + (\mathbf{K}_i^T \mathbf{S_O^{-1}} \mathbf{K}_i + \mathbf{S_A^{-1}})^{-1} \mathbf{K}_i^T \mathbf{S_O^{-1}} [y - \mathbf{F}(\mathbf{x}_i) + \mathbf{K}_i(\mathbf{x}_i - \mathbf{x_A})] \quad (2)$$

165   Where $\mathbf{S_O} = [\boldsymbol{\varepsilon\varepsilon}^T]$ is the observation error covariance matrix defined by the instrument signal to noise

166   ratio (SNR), $\mathbf{x_A}$ is the prior estimate of the state vector, and $\mathbf{S_A}$ is the prior error covariance matrix.

167   The matrix $\mathbf{K}$, or Jacobian matrix, represents the first derivative of the $\mathbf{F}(\mathbf{x})$ with respect to the state

168   vector:

169          $$\mathbf{K}_i = \left.\frac{\partial \mathbf{F}}{\partial \mathbf{x}}\right|_{\mathbf{x}=\mathbf{x}_i} \quad (3)$$

170   The posterior error covariance matrix can be computed explicitly to quantify retrieval precision:

171          $$\hat{\mathbf{S}} = \left(\mathbf{K}_i^T \mathbf{S_O^{-1}} \mathbf{K}_i + \mathbf{S_A^{-1}}\right)^{-1} \quad (4)$$

172   Across the scenes we acquired with PRISMA, using this retrieval approach, we quantify an

173   average 3.3 ppm precision for an XCO_2 column. Absolute biases in PRISMA XCO_2 retrievals are

174   less important for CO_2 plume detection and quantification: systematic retrieval biases are removed

175   from a scene through the quantification and removal of a local background, as described below. To

176   characterize bias in emission quantification, we compare emission rates derived from PRISMA to

177   stack-level CEMS measurements (Section 3.2).

178   We quantified emissions for each PRISMA plume detection using the Integrated Mass

179   Enhancement (IME) approach (Cusworth et al., 2021). However, we updated the masking scheme

180   for this analysis to produce more reliable masks for each CO_2 plume. Figure 1 shows the plume

181   masking procedure for a plume detected at the Hekinan, Japan power plant on July 19, 2021. First,

182   we apply a background threshold to differentiate candidate plume pixels from the background

183   (method to quantify background threshold described in Section 3.2). We then group enhanced XCO_2

184   pixels into clusters of at least 20 connected pixels. These groups are then buffered with a one-pixel

185   dilation filter to smooth edges and any gaps that exist in a group (Dougherty, 1992). Finally, each

186   cluster is considered part of the plume if at least one of its pixels is within 500 m of an exhaust stack.
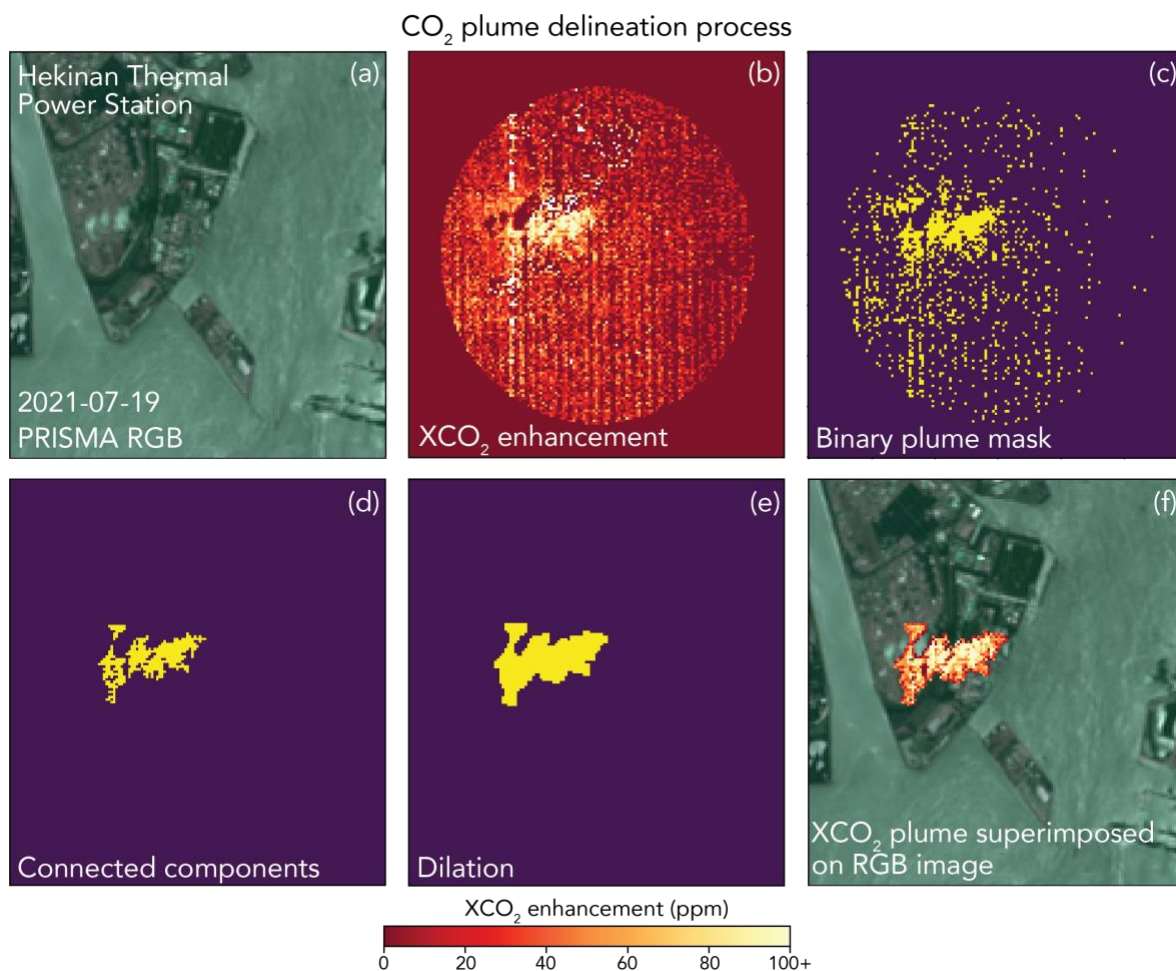
187

188   **Figure 1**. Example of the plume delineation and masking process performed on XCO_2 retrievals

189   derived from PRISMA observations. Panel (a) shows the simultaneously observed RGB PRISMA

190   imagery, panel (b) shows retrieved XCO_2 above the background, panels (c)-(e) show the plume

191   masking procedure to isolate enhanced pixels and remove noise, and panel (f) shows the resulting

192   CO_2 plume superimposed on the RGB imagery.

193

194   IME is calculated for a plume using the following equation:

$$\text{IME} = \sum_{i=1}^{N} \Delta\Omega_i \, \Lambda_i \quad (5)$$

196   where $\Delta\Omega_i$ is the XCO_2 mass enhancement in pixel i relative to background (kg m^{-2}), Λ_i is the pixel

197   area (900 m^2), and N is the number of pixels in the plume. The CO_2 emission rate Q is estimated from

198   the IME using the following relationship:

$$Q = \frac{U_{eff}}{L} \text{ IME} \quad (6)$$

200   where $L = \sqrt{\sum_{i=1}^{N} \Lambda_i}$ is the plume length and U_{eff} is the effective wind speed. The parameter L is an

201   operational parameter that needs to be related to the extent of the plume. Since a plume dissipates in

202   all directions due to turbulent diffusion, an explicit scaling function (i.e., an effective wind speed

203   U_{eff}) that relates L and 10 m wind speed (U_{10}) to the true emission can be derived through large eddy

204   simulations (Varon et al., 2018):

$$U_{eff} = 1.1 \log U_{10} + 0.6. \quad (7)$$

206   where U_{eff} and U_{10} are in units of [m s^{-1}]. We query the ERA5-Land reanalysis using the Open-Meteo

207   Application Programming Interface (open-meteo.com), which provides hourly wind information

208   globally at 0.1° spatial resolution (Muñoz-Sabater et al., 2021). Uncertainty due to winds is calculated

209   by generating an ensemble of U_{10} values assuming 50% error (Cusworth et al., 2021). Uncertainty

210   due to the CO_2 background is calculated by generating many emission estimates and calculating a

211   standard deviation using an ensemble of background thresholds. Background thresholds are set to

212   vary with scene-averaged CO_2 retrieval precision. Total emission uncertainty is estimated by adding

213   in quadrature the contribution of wind and background uncertainties.

214

2.2 OCO-3 observations and quantification

215

216   OCO-3 is also a tasked mission: it can take SAMs over any place of interest within the latitude

217   range of the ISS orbit (about 52° S to 52° N). In addition to the SAM locations we supplied to OCO-

218   3 to overlap with PRISMA targets, there are many other power plant and fossil fuel combustion

219   sources that make up its set of mission targets. However, unlike PRISMA, OCO-3 does not consider

220   cloud forecasts, snow cover, or viewing geometry when planning SAMs and thus the majority of

221   observations fail to produce useful maps of XCO_2. Additionally, aerosol- and albedo-induced XCO2

222   artifacts are present in many SAMs (Bell et al., 2023) and thus make the detection of plumes even

223   more difficult.

224   For all cloud-free soundings, OCO-3 XCO2 concentrations are derived using the

225   Atmospheric Carbon Observations from Space (ACOS; O'Dell et al., 2012; Crisp et al., 2012; O'Dell

226   et al., 2018) v10 optimal estimation retrieval, which employs the Levenberg-Marquardt modification

227   of the Gauss-Newton method. In this work, bias corrected XCO_2 from the OCO-3 Lite files is used

228   but the official data quality flag is not applied. This was done because often the quality flag removes

229   XCO_2 retrievals within the plume and makes emission estimation more difficult or impossible

230   (Nassar et al., 2022). For SAMs where we visually identified CO_2 plumes (e.g., Figure 2), emission

231   rates are estimated using two approaches: (1) a Gaussian plume model and (2) the IME method. For

232   the Gaussian plume model approach, we follow the algorithm outlined in Nassar et al. (2022):

233
$$V(x,y) = \frac{Q}{\sqrt{2\pi}\sigma_y(x)u} e^{-(\frac{1}{2})(\frac{y}{\sigma_y(x)})^2} \quad (8)$$

234
$$\sigma_y(x) = a \cdot \left(\frac{x}{x_o}\right)^{0.894} \quad (9)$$

235 Where V represents the vertical columns within the plume (g/m^2), Q is the CO_2 emission rate (g/s),

236 y is the wind direction perpendicular to the plume (m), u is the wind speed at the height of the plume

237 at its midline (m/s) assuming plume rise of 250 m above the stack height, $\sigma_y(x)$ is the standard

238 deviation of the y-direction, x_o is a characteristic plume length (1000 m), and a is a stability

239 parameter (Nassar et al., 2021). Following Nassar et al. (2022), wind speed and direction inputs are

240 estimated by taking the average of ERA-5 (Bell et al., 2020) and MERRA-2 reanalysis data. The

241 wind direction is optimized by rotating the plume, typically between -30° to 30° away from the mean

242 ERA-5/MERRA-2 direction, and calculating the correlation coefficient (R) of the modeled and

243 observed XCO_2. The optimized wind direction is the direction that produces the largest R. The

244 background is typically estimated by averaging OCO-3 footprints within a radius of 30 km, excluding

245 the plume itself and a narrow 3 km buffer zone. However, if there are visible artifacts in the XCO_2

246 background that are unrelated to the power plant plume, the background field is modified to avoid

247 them. For example, decreasing the radius of footprints used from 30 km to 20 km. The uncertainty

248 in wind speed is calculated by taking the difference of the emission estimate using two different

249 models (ERA-5 and MERRA2). The background concentration uncertainty is calculated by

250 estimating Q using three different background radii of 30, 40, and 50 km. Q is also calculated for a

251 30 km radius background but only using the left and right halves of the background, relative to the

252 direction of the plume. The standard deviation of both these methods is calculated and the larger of

253 the two is the background uncertainty. The plume rise uncertainty is calculated by estimating Q using

254 plume rise values of 100, 200, 250, 300, and 400 m and taking the standard deviation of those values.

255 Total uncertainty on the emission rate Q using the Gaussian plume method is estimated by adding in

256 quadrature the contribution of wind speed, background concentration, and plume rise uncertainties.

257   To obtain another estimate of emission rate, we also apply an IME quantification approach to

258   the CO_2 plumes, which to our knowledge is the first time the IME method has been applied to OCO-

259   3 SAMS at coal power plants. We first interpolate the XCO_2 retrievals in a SAM to a uniform 2×2

260   km^2 grid to account for occasional OCO-3 footprint overlap. Similar to Varon et al. (2018), 3×3

261   pixel neighborhoods are sampled and the distributions are compared to the background using a

262   Student's *t*-test. The default confidence level for the *t* test is 95% but this is often lowered to visually

263   capture most of the plume. The plume is then smoothed using a 3×3 pixel median filter and a

264   Gaussian filter with a standard deviation of 0.5. The U_{eff} calculation is done using an equation

265   approximately equal to Equation 7 ($U_{eff} = 1.0 \log U_{10} + 0.55$). Other recent studies have used various

266   methods (Lin et al., 2023; Brunner et al., 2023), but further research is needed to determine the most

267   accurate way to estimate U_{eff} for an OCO-3-like instrument. The wind direction is the optimized

268   direction determined by the Gaussian plume model. The background XCO_2 estimate is taken from

269   the Gaussian plume model methodology and the plume is typically required to be within 50 km

270   downwind and 8 km crosswind of the source, although these parameters are modified if the plume

271   curves outside of the 8 km crosswind threshold or there are XCO_2 artifacts that should be avoided.

272   The uncertainty for the IME method is estimated similarly to the Gaussian plume model

273   method. The uncertainty in wind speed is calculated by taking the standard deviation of the emission

274   estimates using wind speed from two different models (ERA-5 and MERRA2). The background

275   concentration uncertainty is calculated by estimating Q using the different backgrounds calculated in

276   the Gaussian plume model method: a 20 km radius, 30 km radius, 40 km radius, left half, full circle,

277   and right half. The standard deviation of the three radii estimates and left half, full circle, and right

278   half estimates are calculated and the larger of the two is the background uncertainty. Uncertainty of

279   the Student's *t*-test confidence level is also estimated. The confidence level and -10% and +10% of

280   the confidence level are used to find Q. For example, if the confidence level needed to visually

281   capture the XCO_2 plume is 85%, Q is calculated for 75%, 85%, and 95% and the standard deviation

282   of those three values represents the confidence level uncertainty. Total uncertainty on the emission

283   rate Q using the IME method is estimated by adding in quadrature the contribution of wind speed,

284   background concentration, and Student's t-test confidence level uncertainties.

285   Figure 2 shows IME methodology successfully identifying an XCO_2 plume from an OCO-3

286   SAM taken over the Colstrip power plant.
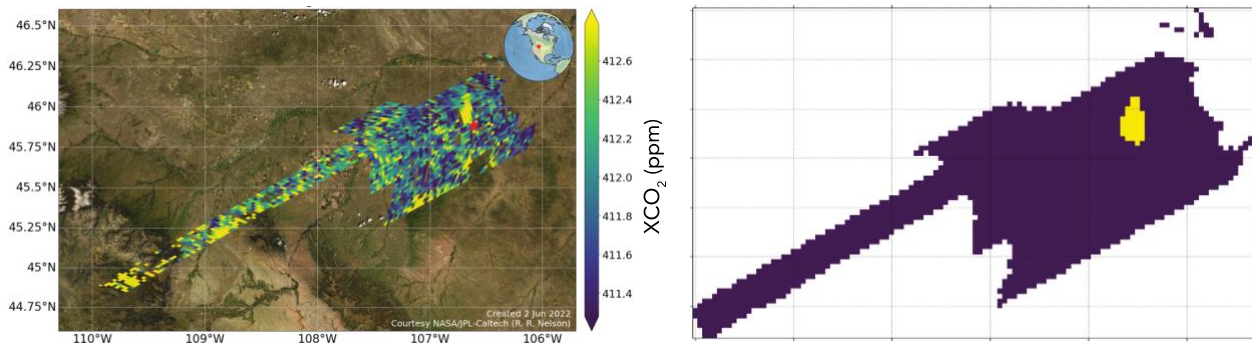
287

288   **Figure 2.** IME plume identification approach applied to an example OCO-3 SAM at the Colstrip

289   power plant on 18 August 2021. Left panel: OCO-3 SAM bias corrected XCO_2. Right panel: yellow

290   pixels indicate the final plume mask.

291

292   **3 Results**

293   *3.1 Global yields from two years of observations*

294   Figure 3a shows a global map of power plants we targeted with PRISMA, with the marker

295   for each power plant's location (latitude, longitude) scaled to represent the number of successful

296   acquisitions between 2021-2022. In total, we acquired 181 PRISMA images, which corresponds to

297   314 unique power plant observation scenes. Of these scenes, 210 were of sufficient quality to attempt

298 CO_2 retrieval and plume detection, with quality mostly determined by visual inspection for clouds

299 and haze. Of these 210 scenes, 104 were determined to have CO_2 plumes (Figure 3b). Scenes were

300 marked as containing CO_2 plumes through inspection of XCO2 and visible imagery: if a large cluster

301 of pixels with elevated XCO_2 above the background were also in the vicinity of a power plant exhaust

302 stack, an analyst would mark the scene as containing a CO_2 plume. Routine tasking observations with

303 PRISMA resulted in an average of 6 acquisitions for each power plant (maximum 15), roughly one

304 image acquired per quarter. Of these acquisitions, plumes were detected on average four times per

305 facility (maximum 12).

306   For OCO-3, 1363 power plant SAMs were taken during September 2019 to December 2022.

307 Of these, 139 XCO_2 plumes emanating from power plants were visually identified. However, only

308 14 were for power plants that were also observed by PRISMA and have CEMS validation (nine

309 Colstrip cases, two Martin Lake cases, and three Craig cases). The acquisition rates are low relative

310 to PRISMA because OCO-3 does not account for scene favorability when planning its SAMs. For

311 example, OCO-3 took 66 Colstrip SAMs from 2019-2022 yet only yielded nine high-quality XCO_2

312 plume cases.
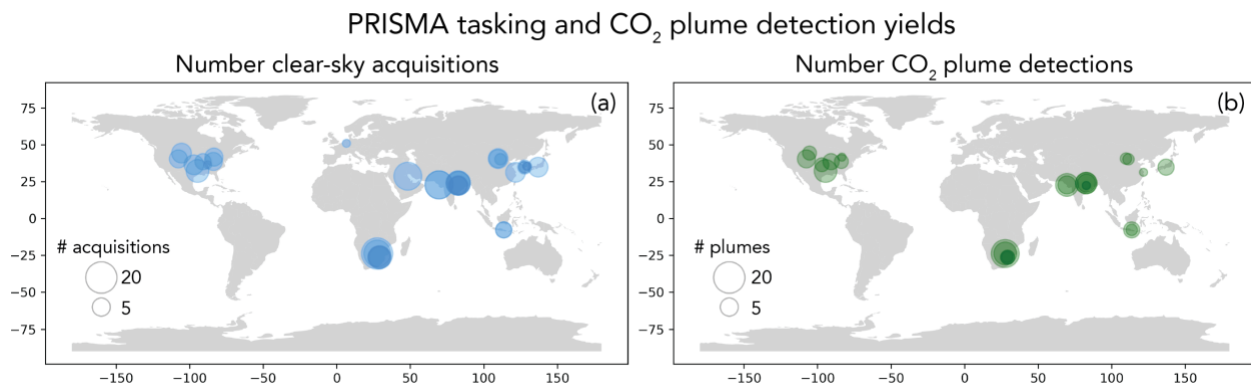
313

314 **Figure 3**. Data yields from PRISMA continually between 2021-2022. Panel (a) shows the number

315 of clear-sky acquisitions for each power plant. Panel (b) shows the number of plumes detected by an

316 analyst for each of the observed power plants.

317

318 The low observed average detection rate of CO_2 plumes is a result of three primary factors:

319 (1) observing conditions at each facility including solar zenith angle (SZA) and surface reflectance;

320 (2) local meteorology; and (3) operational status at each power plant at the time of acquisition. To

321 test how well these factors predict the presence of a plume for PRISMA, we fit a logistic regression

322 classification function with a sparse (L1) penalty to our dataset (Fan et al., 2008). This algorithm fits

323 a logit function to the plume detection outcome of each scenes (i.e., detected plume = TRUE, no

324 detected plume = FALSE) using a set of predictor variables that are likely candidates to explain

325 prediction results. In this setup, the statistical model is fit using the following predictor variables –

326 SZA, U_{10}, average single-sounding retrieval precision across the scene, annual bottom-up emission

327 estimate for the power plant using GEM, and average observed radiance between 1900-2100 nm

328 within the scene normalized by the cosine of the SZA. This last factor is a simple proxy for surface

329 reflectance, although it does not take into account other factors that influence radiance observations

330 (e.g., water vapor, aerosols, other atmospheric constituents). We split the data so that 50% was used

331 to train the model and 50% was reserved as a test set. The predictor variables were all standardized

332 by their mean and standard deviation before the model was fit. The results of classification can be

333 summarized using two statistics: precision (ratio of true positives to sum of true positives and false

334 positives) and recall (ratio of true positives to sum of true positives and false negatives). The results

335 of fitting a logistic regression model to the data show minor prediction performance, with precision

336 = 0.60 and recall = 0.69 for positive plume detection. The regression coefficients are shown in Figure

337   4a. The coefficient with the highest weight is normalized radiance. Figure 4b shows SZA against

338   normalized radiance, with red dots indicating no plume detection and blue dots representing positive

339   plume detection. Though no clear separation exists, there is a cluster of no plume detection at high

340   SZA and low normalized radiance. This is a consistent and expected relationship, as SZA and surface

341   reflectance are principal drivers of the quantity of light that is observed by the satellite, and therefore

342   SNR of the observation.

343
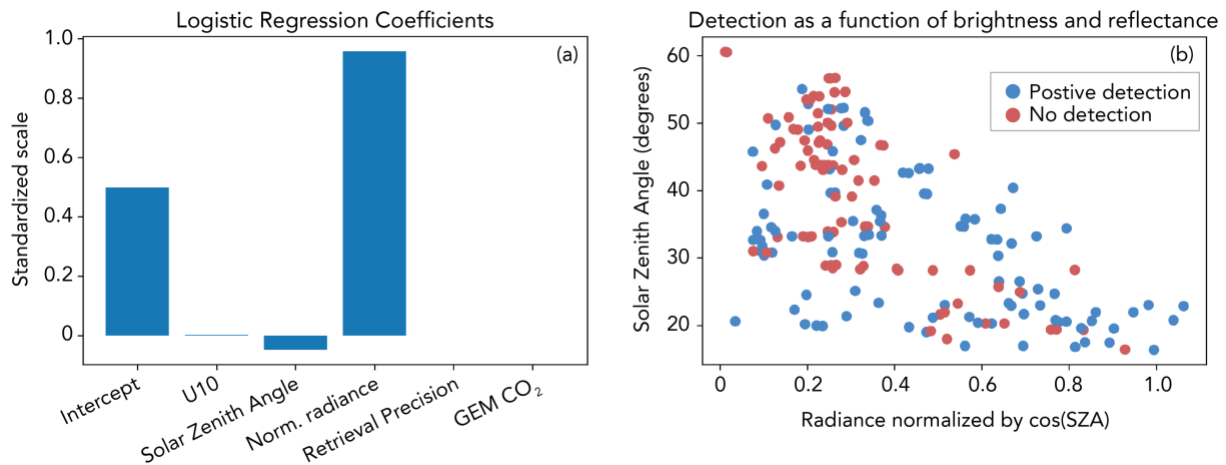
344

345   **Figure 4**. CO_2 plume prediction using various atmospheric, retrieval, and bottom-up information.

346   Panel (a) shows the results of fitting a logistic regression classification model to the set of PRISMA

347   acquisitions where an analyst identified the presence or lack of a plume. Panel (b) shows the top two

348   explanatory variables (SZA and normalized radiance) along with plume classification.

349

350   The logistic regression model performed better on the test data set than predictions made at

351   random, though the prediction performance was still low. Missing from the model is sub-annually

352   resolved information regarding operating status. For most of the power plants outside the U.S., we

353   do not have information on daily operations of a power plant. In many cases of non-detects, we could

354   simply be observing a power plant temporarily not in operation. Another possibility is that at the time

355   of acquisition, some power plants were operating at reduced capacity, meaning that CO_2 emission

356   rates were lower than those predicted by annual emission factors or activity data. If the true CO_2

357   emission rate was below the minimum detection limit (MDL) possible by the PRISMA satellite, then

358   it would show as a non-detect. However, even if the emission were near or slightly above the

359   PRISMA MDL, the probability of detection would still be low as slight variations in atmospheric

360   properties, as seen in Figure 4, would then influence the ability to detection a CO_2 plume.

361

362   *3.2 Validation of PRISMA and OCO-3 emission rates against CEMS*

363   For each power plant where a CO_2 plume was identified, we quantify emissions using the

364   IME approach described by Equations 5-7. In order to estimate the XCO_2 mass enhancement ($\Delta\Omega$ in

365   Equation 1), a local background must be quantified and subtracted from total XCO_2 retrievals across

366   the scene. To do this, we apply a concentration threshold β to initiate the plume masking and

367   segmentation process (described in Methods section). Once we have a plume mask, we apply another

368   concentration threshold γ to the remaining XCO_2 pixels that exist outside of the plume. This value γ

369   represents the XCO_2 background that we use to calculate the XCO_2 enhancement that is used in the

370   IME formulation of Equation 1. Thresholds β and γ largely influence the magnitude of the emission

371   rate and are not known a priori. For global generalizability, we wish to estimate β and γ such that

372   they do not vary across power plants, seasons, regions, etc. Therefore, we parameterize β and γ as

373   percentiles under the assumption that the local contrast between enhanced CO_2 plume pixels and the

374   background should be similar across PRISMA scenes.

375   To estimate values for β and γ, we compare EPA CEMS data for power plants in the U.S.

376   with estimated emission rates from PRISMA. In total, we have 12 scenes in the U.S. with CEMS

377   information that pertain to 5 power plants. We then optimize β and γ such that the output of an

378   ordinary least squares regression produces a slope near unity. Figure 5a shows the results of this

379   optimization which produces an optimal β percentile of 94% and a γ percentile of 62%. The results

380   also show decent correlation between CEMS data and PRISMA-derived emission rates ($R^2 = 0.43$).

381   A single outlier at the Labadie power plant (imaged July 10, 2022) shows the largest discrepancy

382   from CEMS data (69%), but the remaining plumes show average 27% relative difference from CEMS

383   data. If we remove the one data point at Labadie, the R^2 improves to 0.75. Though a limited sample

384   size, between PRISMA and OCO-3, these scenes represent variability in solar geometries (20-40°

385   SZA), surface reflectance (0.09-0.90 normalized radiance), and reported emission rates (0.51 – 2.39

386   kt CO2 h^{-1}). Therefore, we use these optimal parameters and apply them to our global dataset of

387   PRISMA detections. These emission rates are reported in Table 1. There are some instances when

388   performing IME emission calculations using these thresholds and plume masking technique do not

389   result in emission rates (e.g., the plume masking procedure produces a mask with no pixels). In these

390   cases, we report a detection but not an emission quantification.

391   Figures 5b and 5c shows the comparison between OCO-3 and CEMS at some power plants

392   that overlap with PRISMA observations (14 scenes total). OCO-3 Gaussian plume model emission

393   rates (Fig. 5b) have an improved correlation compared to PRISMA ($R^2 = 0.51$), although with greater

394   bias (average 47% relative difference from CEMS). The OCO-3 IME estimates (Fig. 5c) have worse

395   R^2 (0.32) but a better RMSE (0.45 kt CO_2/hr) compared to the Gaussian plume model estimates (0.84

396   kt CO2/hr), with 9 of the 14 cases being within 30% of the reported CEMS emission and an average

397   relative difference of 30% for all 14 cases. Additionally, the least squares fit for IME is closer to the

398   1-to-1 line than for the Gaussian plume model.

399
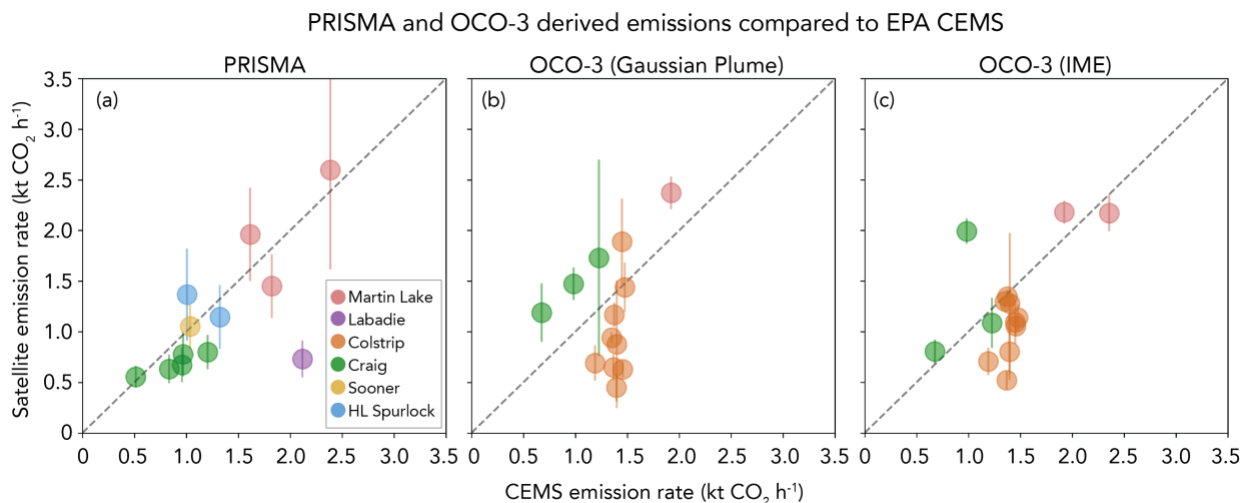
Figure 5. Comparison of emission rates in the U.S. between satellite-derived estimates and CEMS information. Panel (a) shows a comparison between PRISMA derived emission rates and CEMS (R^2 = 0.43), panel (b) shows a comparison between OCO-3 and CEMS using the Gaussian plume model (R^2 = 0.51), and panel (c) shows a comparison between OCO-3 and CEMS using IME (R^2 = 0.32).

Unique sources of error for OCO-3 emission estimates include geolocation errors in the XCO2 product. These errors are typically less than 1 km, but can be up to 2 km (Taylor et al., 2023). Errors of this magnitude, about the size of an OCO-3 footprint ($\sim2\times2$ km^2), may mean that an entire footprint is not included when estimating emissions using the Gaussian plume method, which assumes that the plume only extends downwind of the known source location. The Gaussian plume model is also susceptible to wind direction errors, and requires the plume to be Gaussian in shape, which is often not true. IME, while not suffering from wind direction or geolocation-induced errors, assumes that the entire plume is captured in a given SAM, which is sometimes not true and results in an underestimation of emissions. IME is also sensitive to errors in U_{eff} parameterization.

416 *3.3 Comparison and fusion of PRISMA and OCO*

417   Outside the U.S., PRISMA observed the Matimba power station in South Africa 11 times and

418 quantified emission rates 7 times. Emissions from Matimba have previously been quantified and

419 validated using OCO-2 (Hakkarainen et al., 2021). This station does not report hourly emission rates,

420 but does report daily power generation (Eskom, 2023). Though not a direct comparison, we can use

421 this information to check if the emission quantification approach we describe above captures some

422 variability in activity at this power plant. Figure 6a shows the emission rates we quantified compared

423 against reported power generation. We see rough agreement in variability – the high power

424 generation reported between Apr to July 2021 (70000-85000 MWh) drop for subsequent dates

425 (47000-66000 MWh) between Sep 2021 to Sep 2022, a drop which is also seen in the PRISMA-

426 derived CO2 emission rate. Across all observations, we estimate an emission rate range of 0.30-1.04

427 kt CO2 h^{-1} (average 0.66 kt CO_2 h^{-1}). This average emission rate is substantially lower than the

428 average 2.50 kt CO_2 h^{-1} emission rate estimated from OCO-2 and TROPOMI between 2018-2020,

429 but within the range of emissions estimates directly quantified with OCO-2 (0.30-7.20 kt CO_2 h^{-1};

430 Hakkarainen et al., 2021). However, this discrepancy could be result of (1) changes in activity or

431 variability or (2) existence of other nearby emission sources. For changes in activity, during August

432 2020, the Matimba reported a large range of power generation (65000-94000 MWh) and emission

433 estimates derived directly from OCO-2 were also highly variable (0.88-4.33 kt CO_2 h^{-1}). Given that

434 maximum power generation at the time of a PRISMA observation was 85000 MWh, some of the

435 discrepancy in maximum CO_2 quantification between PRISMA and OCO-2 could be due to activity.

436   Nearby (7 km) the Matimba Power Station is the Medupi Power Plant (Figure 6b). Figure 6c

437 show the Medupi CO_2 plume observed during the same PRISMA overpass on Apr 5, 2021. The

438 PRISMA derived emission rate for Medupi is 0.64 ± 0.26 kt CO2 h^{-1} and for Matimba is 0.73 ± 0.30

439   kt CO_2 h^{-1}. Given the proximity of the two power plants, the higher derived emission rate reported

440   for Matimba from previous studies could actually be a result of a net emission from these two

441   facilities. The OCO-2 flight track is located tens of kilometers downwind from Matimba and Medupi,

442   making a clear delineation between potentially co-emitted distinct emission plumes near impossible.

443   If we sum emission rates from both Medupi and Matimba, we quantify a range of 0.89-1.73 kt CO_2

444   h^{-1} (1.30 $\pm$ 0.28 kt CO2 h^{-1}), which is still lower, but closer to the average emissions quantified by

445   OCO-2.
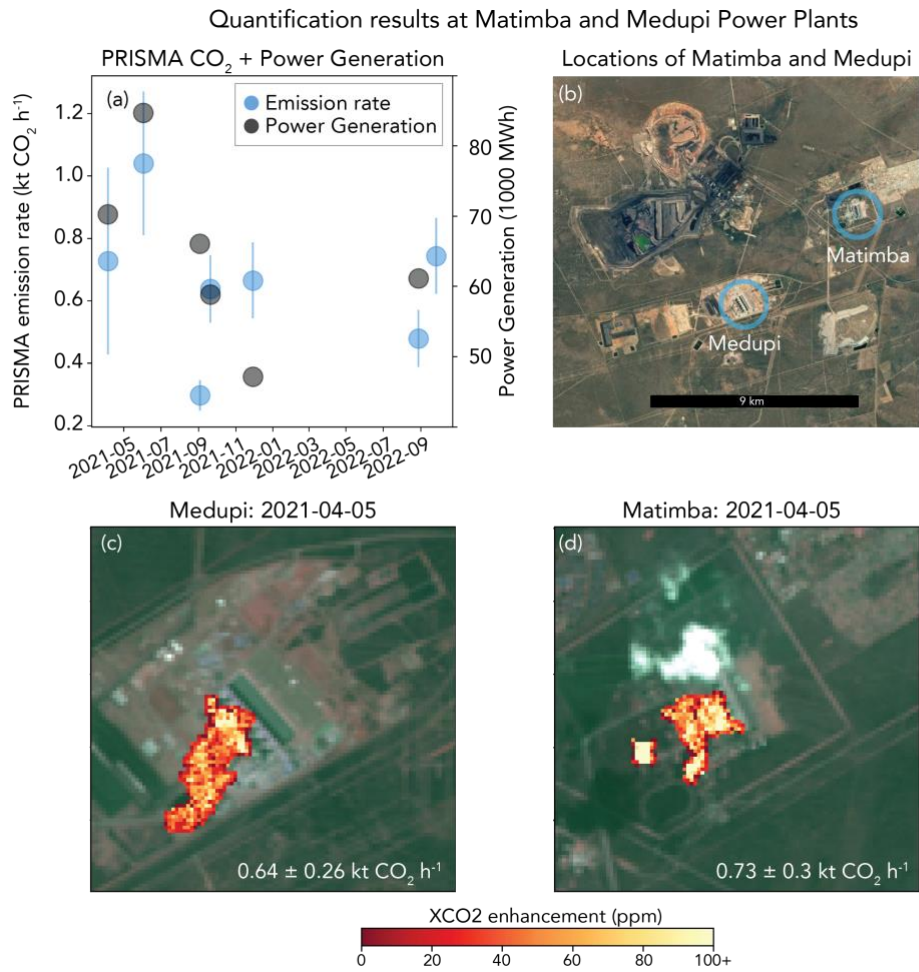
446

447   **Figure 6**. Emission rates and reported power generation at the Matimba and Medupi power plants in

448   South Africa. Panel (a) shows the CO2 emission rates derived from PRISMA and the reported daily

449   power generation for the day of PRISMA overpass. Panel (b) shows the locations of the Medupi and

450   Matimba power plants (base imagery provided by Google Earth; © Google Earth 2023). Panels (c)

451   and (d) show plume imagery and emission rates for a PRISMA overpass on Apr 5, 2021.

452

453   The ability to differentiate the contribution of unique point sources to a regional total is an

454   application made possible by joint observing of imaging spectrometers and atmospheric sounders.

455   Figure 7 shows observations that were made at the Tata Mundra Ultra Mega Power Plant and the

456   Adani Mundra Thermal Power Project: two power plants less than 3 km apart. Both OCO-3 and

457   PRISMA imaged the power plants on Apr 9, 2022. Figure 7b shows the OCO-3 SAM (taken 04:41

458   UTC) – large CO_2 enhancements appear along the coastline likely associated with emission from

459   these power plants. PRISMA imaged the power plants less than two hours later (06:02 UTC) and

460   detected CO2 plumes at each facility (Figure 7b-c). The OCO-3 derived emission rate using Gaussian

461   plume approaches is 5.5 ± 0.7 kt CO_2 h^{-1}, but the emission rate derived using the IME approach is

462   much lower (3.0 kt CO_2 h^{-1}). For this case, the IME approach may be more appropriate as the shape

463   of the OCO-3 plume (Figure 7b) is more diffuse in nature and does not visibly resemble a Gaussian

464   structure. The PRISMA emission rate for the Adani plant is 1.07 ± 0.17 kt CO_2 h^{-1} and for the Tata

465   Mundra plant is 0.53 ± 0.08 kt CO_2 h^{-1}. We can use this information to estimate that 67% of the net

466   CO_2 emission came from Adani, and the remaining 33% came from the Tata plant. The combined

467   emission rate (1.60 ± 0.25 kt CO_2 h^{-1}) is lower than the OCO-3 IME emission rate. Like the Matimba

468   power plant, some of this discrepancy may partially be explained by bias or uncertainty in retrievals,

469   background, and wind information. Also, lower estimates of CO_2 emissions from PRISMA are

470   consistent with the fact that PRISMA is only sensitive to emissions at two exhaust stacks, while the

471   OCO-3 observation includes all CO_2 sources in the industrial area around Mundra. Continued

472 validation of retrieved emission rates against ground standards (e.g., CEMS) will help better quantify

473 bias and uncertainty. However, even with lingering uncertainty, the near simultaneous observations

474 of OCO-3 and PRISMA can help us disentangle the relative contributions from each power plant.

475
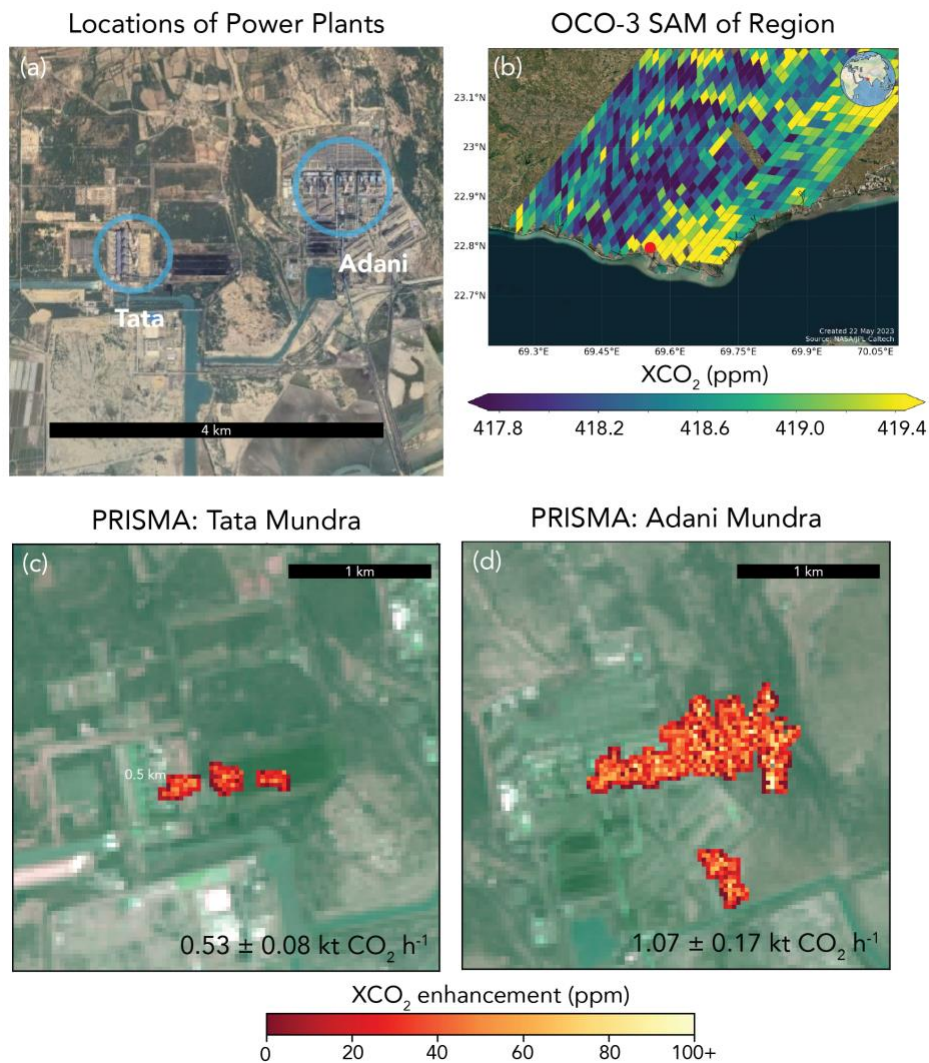
476

477 **Figure 7**. Near-simultaneous observation of two power plants in Mundra, India on Apr 9, 2022. Panel

478 (a) shows the locations of two power plants spaced less than 3 km apart: Tata Mundra and Adani

479 Mundra Power Stations (base imagery provided by Google Earth; © Google Earth 2023). Panel (b)

480 shows the OCO-3 SAM with a red dot showing the location of the power plants. Panel (c) and (d)

481 show the PRISMA acquisition (less than 2 hours after OCO-3) over the two power plants with

482 associated emission rates.

483

484 **Conclusion**

485   We observed a global set of power plants for two years between 2021-2022 with both

486 PRISMA and OCO-3 to test the ability of these satellite platforms to do routine operational

487 monitoring of CO_2 emissions. When PRISMA observations were of sufficient quality to perform

488 XCO_2 retrievals, we detected CO_2 plumes nearly half of the time. We fit a logistic regression

489 classification using plume detections and find that there is some relationship between SZA and

490 surface reflectance that partially explains plume prediction; consistent given that these factors are

491 major drivers of SNR. The remaining non-plume detections may be due to operational status of a

492 power plant at the time of observation. We compared emission rates from both PRISMA and OCO-

493 3 to power plants in the U.S. where we have access to hourly *in situ* CEMS emission information.

494 We find significant correlation between satellite and *in situ* estimates, though some significant biases

495 may exist for some of the observations for both PRISMA and OCO-3. Also, the quantity of CEMS

496 observations was limited (~10 for each instrument), so robust calibration is not yet possible. Still,

497 early results show that under the right conditions, satellites can provide reliable estimates of CO_2

498 emissions at discrete point source locations. This is consistent with the close agreement between

499 airborne imaging spectrometer emissions and CEMS information (Cusworth et al., 2021).

500   Fusion of information from atmospheric sounders like OCO-3 and imaging spectrometers

501 like PRISMA is valuable for cross-validation and source attribution. We see this particularly for our

502 examples at the Matimba and Medupi power plants in South Africa and the Tata and Adani power

503   plants in Mundra, India. In these cases, and particularly at Mundra where near-simultaneous

504   PRISMA and OCO-3 observations were taken, OCO-2/3 provides a local, but coarse resolution

505   emission constraint for a complex of facilities that emit large CO_2 quantities. PRISMA, with its 30

506   m pixel resolution, then can help refine relative contributions of single emitters against the net

507   emission flux. More work is needed to refine cross-validation between instruments, but initial

508   observation shows one avenue for data from multiple observing systems to be complementary

509   aggregated and analyzed.

510   Even when combining information from both satellites, there is still too little sampling to

511   constrain facility emissions within low uncertainties. Cusworth et al. (2021), using arguments from

512   Hill and Nassar (2019), suggested that nearly 30 unbiased observations from a PRISMA-class

513   instrument is needed per year at each power plant to reduce annual uncertainties below 14% (i.e.,

514   reduce emission uncertainty from Non-Annex I countries below 1 Gt CO_2 per year). No power plant

515   in this study met this minimum sampling requirement. However, there will be a significant increase

516   in data volumes and observation performance of satellite remote sensing capabilities for CO2, from

517   both recently launched and planned imaging spectrometers including EMIT (launched 2022; Thorpe

518   et al., in revision); EnMAP (launched 2022; Guanter et al., 2015); Carbon Mapper/Tanager 1-2

519   (Planned launch 2024; Duren et al., 2021), and atmospheric sounders including CO2M (Sierk et al.,

520   2019). Improved observation of global power plants and emission quantification with robust error

521   characterization will be vital to reduce global uncertainty of anthropogenic emissions from fossil fuel

522   combustion sources.

523

524   **Data Availability**.

525   The OCO-3 XCO2 and other retrieval properties are publicly available at the NASA Goddard Earth

526   Science Data and Information Services Center (GES-DISC). The full suite of retrieval products in

527   the standard per-orbit format can be obtained at OCO Science Team et al., 2021,

528   https://doi.org/10.5067/D9S8ZOCHCADE. The lightweight per-day format data (Lite files), which

529   includes the bias corrected estimates of XCO2, can be obtained at OCO Science Team et al., 2022,

530   https://doi.org/10.5067/970BCC4DHH24. PRISMA data including radiance for each scene and

531   XCO2 retrievals is available at https://doi.org/10.5281/zenodo.8083596.

532

533   **Acknowledgments**. This work was supported by the Orbiting Carbon Observatory Science Team.

534   We thank the Italian Space Agency for the PRISMA satellite targets. Portions of this work were

535   undertaken at the Jet Propulsion Laboratory, California Institute of Technology, under contract with

536   NASA.

537

538   **Author Contributions**. DHC designed the study. DHC, AKA, RJ tasked and acquired PRISMA

539   data. DHC performed PRISMA emission quantification and validation. RRN performed OCO-3

540   quantification and validation. RN and JPM helped implement OCO-3 quantification algorithms. All

541   authors provided feedback on results and the manuscript.

542

543

544   **Competing interests**. The authors declare no conflicts of interest.

545

546   **References**

547 Beirle, S., Borger, C., Dörner, S., Eskes, H., Kumar, V., de Laat, A. and Wagner, T., 2021. Catalog

548 of NOx emissions from point sources as derived from the divergence of the NO2 flux for

549 TROPOMI. *Earth System Science Data*, *13*(6), pp.2995-3012. DOI https://doi.org/10.5194/essd-13-

550 2995-2021

551

552 Bell, B., Hersbach, H., Berrisford, P., Dahlgren, P., Horányi, A., Sabater, M., et al.

553 (2020). ERA5 hourly data on pressure levels from 1950 to 1978 (preliminary

554 version). Copernic. Clim. Change Serv. (C3S) Clim. Data Store (CDS). AvaliableAt:

555 https://cds.climate.copernicus-climate.eu/cdsapp#!/dataset/reanalysis-era5-

556 pressure-levels-preliminary-back-extension?tab=overview.

557

558 Bell, E., O'Dell, C.W., Taylor, T.E., Merrelli, A., Nelson, R.R., Kiel, M., Eldering, A., Rosenberg,

559 R. and Fisher, B., 2023. Exploring bias in the OCO-3 snapshot area mapping mode via geometry,

560 surface, and aerosol effects. *Atmospheric Measurement Techniques*, *16*(1), pp.109-133. DOI

561 https://doi.org/10.5194/amt-16-109-2023

562

563 Brunner, D., Kuhlmann, G., Henne, S., Koene, E., Kern, B., Wolff, S., Voigt, C., Jöckel, P.,

564 Kiemle, C., Roiger, A. and Fiehn, A., 2023. Evaluation of simulated CO2 power plant plumes from

565 six high-resolution atmospheric transport models. *Atmospheric Chemistry and Physics*, *23*(4),

566 pp.2699-2728. DOI https://doi.org/10.5194/acp-23-2699-2023

567

568 Crippa, M., Guizzardi, D., Banja, M., Solazzo, E., Muntean, M., Schaaf, E., Pagani, F., Monforti-

569 Ferrario, F., Olivier, J., Quadrelli, R., Risquez Martin, A., Taghavi-Moharamli, P., Grassi, G.,

570   Rossi, S., Jacome Felix Oom, D., Branco, A., San-Miguel-Ayanz, J. and Vignati, E., CO2

571   emissions of all world countries - 2022 Report, EUR 31182 EN, Publications Office of the

572   European Union, Luxembourg, 2022, doi:10.2760/730164, JRC130363

573   Crisp, D., Fisher, B.M., O'Dell, C., Frankenberg, C., Basilio, R., Bösch, H., Brown, L.R., Castano,

574   R., Connor, B., Deutscher, N.M. and Eldering, A., 2012. The ACOS CO2 retrieval algorithm–part

575   II: global XCO2 data characterization. *Atmospheric Measurement Techniques*, *5*(4), pp.687-707.

576   DOI https://doi.org/10.5194/amt-5-687-2012

577

578   Cusworth, D.H., Duren, R.M., Thorpe, A.K., Eastwood, M.L., Green, R.O., Dennison, P.E.,

579   Frankenberg, C., Heckler, J.W., Asner, G.P. and Miller, C.E., 2021. Quantifying global power plant

580   carbon dioxide emissions with imaging spectroscopy. *AGU Advances*, *2*(2), p.e2020AV000350.

581   DOI https://doi.org/10.1029/2020AV000350

582

583   Dougherty, E.R., 1992. An introduction to morphological image processing. In *SPIE*. Optical

584   Engineering Press.

585

586   Duren, R., Cusworth, D., Ayasse, A., Herner, J., Thorpe, A., Falk, M., Heckler, J., Guido, J.,

587   Giuliano, P., Chapman, J. and Green, R., 2021, December. Carbon Mapper: on-orbit performance

588   predictions and airborne prototyping. In *AGU Fall Meeting Abstracts* (Vol. 2021, pp. A53F-05).

589

590   Eldering, A., Taylor, T.E., O'Dell, C.W. and Pavlick, R., 2019. The OCO-3 mission: measurement

591   objectives and expected performance based on 1 year of simulated data. *Atmospheric Measurement*

592   *Techniques*, *12*(4), pp.2341-2370. DOI https://doi.org/10.5194/amt-12-2341-2019

593

594 Fan, R.E., Chang, K.W., Hsieh, C.J., Wang, X.R. and Lin, C.J., 2008. LIBLINEAR: A library for

595 large linear classification. *the Journal of machine Learning research*, *9*, pp.1871-1874. DOI

596 https://doi.org/10.5555/1390681.1442794

597

598 Gelaro, R., McCarty, W., Suárez, M.J., Todling, R., Molod, A., Takacs, L., Randles, C.A.,

599 Darmenov, A., Bosilovich, M.G., Reichle, R. and Wargan, K., 2017. The modern-era retrospective

600 analysis for research and applications, version 2 (MERRA-2). *Journal of climate*, *30*(14), pp.5419-

601 5454. https://doi.org/10.1175/JCLI-D-16-0758.1

602

603 GEM, Global Energy Monitor's Global Coal Plant Tracker, URL

604 https://globalenergymonitor.org/projects/global-coal-plant-tracker/tracker/, last accessed May 24,

605 2023

606

607 Guan, D., Liu, Z., Geng, Y., Lindner, S. and Hubacek, K., 2012. The gigatonne gap in China's

608 carbon dioxide inventories. *Nature Climate Change*, *2*(9), pp.672-675. DOI

609 https://doi.org/10.1038/nclimate1560

610

611 Guanter, L., Kaufmann, H., Segl, K., Foerster, S., Rogass, C., Chabrillat, S., Kuester, T., Hollstein,

612 A., Rossner, G., Chlebek, C. and Straif, C., 2015. The EnMAP spaceborne imaging spectroscopy

613 mission for earth observation. *Remote Sensing*, *7*(7), pp.8830-8857. DOI

614 https://doi.org/10.3390/rs70708830

615

616   Guo, W., Shi, Y., Liu, Y. and Su, M., 2023. CO2 emissions retrieval from coal-fired power plants

617   based on OCO-2/3 satellite observations and a Gaussian plume model. *Journal of Cleaner*

618   *Production*, *397*, p.136525. DOI https://doi.org/10.1016/j.jclepro.2023.136525

619

620   Hakkarainen, J., Szeląg, M.E., Ialongo, I., Retscher, C., Oda, T. and Crisp, D., 2021. Analyzing

621   nitrogen oxides to carbon dioxide emission ratios from space: A case study of Matimba Power

622   Station in South Africa. *Atmospheric Environment: X*, *10*, p.100110. DOI

623   https://doi.org/10.1016/j.aeaoa.2021.100110

624

625   Hill, T. and Nassar, R., 2019. Pixel size and revisit rate requirements for monitoring power plant

626   CO2 emissions from space. *Remote Sensing*, *11*(13), p.1608. DOI

627   https://doi.org/10.3390/rs11131608

628

629   Hong, C., Zhang, Q., He, K., Guan, D., Li, M., Liu, F. and Zheng, B., 2017. Variations of China's

630   emission estimates: response to uncertainties in energy statistics. *Atmospheric Chemistry and*

631   *Physics*, *17*(2), pp.1227-1239. DOI https://doi.org/10.5194/acp-17-1227-2017

632

633   IPCC, 2021: *Climate Change 2021: The Physical Science Basis. Contribution of Working Group I*

634   *to the Sixth Assessment Report of the Intergovernmental Panel on Climate Change*[Masson-

635   Delmotte, V., P. Zhai, A. Pirani, S.L. Connors, C. Péan, S. Berger, N. Caud, Y. Chen, L. Goldfarb,

636   M.I. Gomis, M. Huang, K. Leitzell, E. Lonnoy, J.B.R. Matthews, T.K. Maycock, T. Waterfield, O.

637   Yelekçi, R. Yu, and B. Zhou (eds.)]. Cambridge University Press, Cambridge, United Kingdom and

638   New York, NY, USA, In press, doi:10.1017/9781009157896.

639

640   J. Muñoz-Sabater, Dutra, E., Agustí-Panareda, A., Albergel, C., Arduini, G., Balsamo, G.,

641   Boussetta, S., Choulga, M., Harrigan, S., Hersbach, H., Martens, B., Miralles, D. G., Piles, M.,

642   Rodríguez-Fernández, N. J., Zsoter, E., Buontempo, C., and Thépaut, J.-N.: ERA5-Land: A state-

643   of-the-art global reanalysis dataset for land applications, Earth Syst. Sci. Data,13, 4349–4383,

644   2021. https://doi.org/10.5194/essd-13-4349-2021.

645

646   Kochanov, R.V., Gordon, I.E., Rothman, L.S., Wcisło, P., Hill, C. and Wilzewski, J.S., 2016.

647   HITRAN Application Programming Interface (HAPI): A comprehensive approach to working with

648   spectroscopic data. *Journal of Quantitative Spectroscopy and Radiative Transfer*, *177*, pp.15-30.

649   DOI https://doi.org/10.1016/j.jqsrt.2016.03.005

650

651   Lin, X., van der A, R., de Laat, J., Eskes, H., Chevallier, F., Ciais, P., Deng, Z., Geng, Y., Song, X.,

652   Ni, X. and Huo, D., 2023. Monitoring and quantifying CO_2 emissions of isolated power plants

653   from space. *EGUsphere*, pp.1-20. DOI https://doi.org/10.5194/egusphere-2022-1490

654

655   Loizzo, R., Guarini, R., Longo, F., Scopa, T., Formaro, R., Facchinetti, C. and Varacalli, G., 2018,

656   July. PRISMA: The Italian hyperspectral mission. In *IGARSS 2018-2018 IEEE International*

657   *Geoscience and Remote Sensing Symposium* (pp. 175-178). IEEE. DOI https://doi.org/

658   10.1109/IGARSS.2018.8518512

659

660 Nassar, R., Hill, T.G., McLinden, C.A., Wunch, D., Jones, D.B. and Crisp, D., 2017. Quantifying

661 CO2 emissions from individual power plants from space. *Geophysical Research Letters*, *44*(19),

662 pp.10-045. DOI https://doi.org/10.1002/2017GL074702

663

664 Nassar, R., Mastrogiacomo, J.P., Bateman-Hemphill, W., McCracken, C., MacDonald, C.G., Hill,

665 T., O'Dell, C.W., Kiel, M. and Crisp, D., 2021. Advances in quantifying power plant CO2

666 emissions with OCO-2. *Remote Sensing of Environment*, *264*, p.112579. DOI

667 https://doi.org/10.1016/j.rse.2021.112579

668

669 Nassar, R., Moeini, O., Mastrogiacomo, J.P., O'Dell, C.W., Nelson, R.R., Kiel, M., Chatterjee, A.,

670 Eldering, A. and Crisp, D., 2022. Tracking CO2 emission reductions from space: A case study at

671 Europe's largest fossil fuel power plant. *Frontiers in Remote Sensing*, *3*, p.98. DOI

672 https://doi.org/10.3389/frsen.2022.1028240

673

674 O'Dell, C.W., Connor, B., Bösch, H., O'Brien, D., Frankenberg, C., Castano, R., Christi, M.,

675 Eldering, D., Fisher, B., Gunson, M. and McDuffie, J., 2012. The ACOS CO 2 retrieval algorithm–

676 Part 1: Description and validation against synthetic observations. *Atmospheric Measurement*

677 *Techniques*, *5*(1), pp.99-121. DOI https://doi.org/10.5194/amt-5-99-2012

678

679 O'Dell, C.W., Eldering, A., Wennberg, P.O., Crisp, D., Gunson, M.R., Fisher, B., Frankenberg, C.,

680 Kiel, M., Lindqvist, H., Mandrake, L. and Merrelli, A., 2018. Improved retrievals of carbon dioxide

681 from Orbiting Carbon Observatory-2 with the version 8 ACOS algorithm. *Atmospheric*

682 *Measurement Techniques*, *11*(12), pp.6539-6576. DOI https://doi.org/10.5194/amt-11-6539-2018

683

684 Rodgers, C.D., 2000. *Inverse methods for atmospheric sounding: theory and practice* (Vol. 2).

685 World scientific.

686

687 Reuter, M., Buchwitz, M., Schneising, O., Krautwurst, S., O'Dell, C.W., Richter, A., Bovensmann,

688 H. and Burrows, J.P., 2019. Towards monitoring localized CO2 emissions from space: co-located

689 regional CO2 and NO2 enhancements observed by the OCO-2 and S5P satellites. *Atmospheric*

690 *Chemistry and Physics*, *19*(14), pp.9371-9383. DOI https://doi.org/10.5194/acp-19-9371-2019

691

692 Sierk, B., Bézy, J.L., Löscher, A. and Meijer, Y., 2019, July. The European CO2 Monitoring

693 Mission: observing anthropogenic greenhouse gas emissions from space. In *International*

694 *Conference on Space Optics—ICSO 2018* (Vol. 11180, pp. 237-250). SPIE. DOI https://doi.org/

695 10.1117/12.2535941

696

697 Taylor, T.E., O'Dell, C.W., Baker, D., Bruegge, C., Chang, A., Chapsky, L., Chatterjee, A., Cheng,

698 C., Chevallier, F., Crisp, D. and Dang, L., 2023. Evaluating the consistency between OCO-2 and

699 OCO-3 XCO 2 estimates derived from the NASA ACOS version 10 retrieval

700 algorithm. *Atmospheric Measurement Techniques Discussions*, *2023*, pp.1-61. DOI

701 https://doi.org/10.5194/amt-16-3173-2023

702

703 Thorpe, A.K., Frankenberg, C., Thompson, D.R., Duren, R.M., Aubrey, A.D., Bue, B.D., Green,

704 R.O., Gerilowski, K., Krings, T., Borchardt, J. and Kort, E.A., 2017. Airborne DOAS retrievals of

705 methane, carbon dioxide, and water vapor concentrations at high spatial resolution: application to

706   AVIRIS-NG. *Atmospheric Measurement Techniques*, *10*(10), pp.3833-3850. DOI

707   https://doi.org/10.5194/amt-10-3833-2017

708

709   Van Geffen, J., Boersma, K.F., Eskes, H., Sneep, M., Ter Linden, M., Zara, M. and Veefkind, J.P.,

710   2020. S5P TROPOMI NO2 slant column retrieval: Method, stability, uncertainties and comparisons

711   with OMI. *Atmospheric Measurement Techniques*, *13*(3), pp.1315-1335. DOI

712   https://doi.org/10.5194/amt-13-1315-2020

713

714   Varon, D.J., Jacob, D.J., McKeever, J., Jervis, D., Durak, B.O., Xia, Y. and Huang, Y., 2018.

715   Quantifying methane point sources from fine-scale satellite observations of atmospheric methane

716   plumes. *Atmospheric Measurement Techniques*, *11*(10), pp.5673-5686. DOI

717   https://doi.org/10.5194/amt-11-5673-2018